Title

The performance of an inexpensive spark-induced breakdown spectroscopy instrument for near real-time analysis of toxic metal particles

Authors

Li, Hanyang

Mazzei, Leonardo

Wallis, Christopher D

et al.

Publication Date

2021-11-01

DOI

10.1016/j.atmosenv.2021.118666

Peer reviewed

HHS Public Access

Author manuscript

Atmos Environ (1994). Author manuscript; available in PMC 2024 April 23.

Published in final edited form as:

Atmos Environ (1994). 2021 November 01; 264: . doi:10.1016/j.atmosenv.2021.118666.

The performance of an inexpensive spark-induced breakdown spectroscopy instrument for near real-time analysis of toxic metal particles

Hanyang Li[a,*], **Leonardo Mazzei**[b], **Christopher D. Wallis**[a], **Seyyed Ali Davari**[a,1], **Anthony S. Wexler**[a,b,c,d]

[a]Air Quality Research Center, University of California Davis, Davis, CA, 95616, USA

[b]Mechanical and Aerospace Engineering, University of California, Davis, CA, 95616, USA

[c]Civil and Environmental Engineering, University of California, Davis, CA, 95616, USA

[d]Land, Air and Water Resources, University of California, Davis, CA, 95616, USA

Abstract

To meet the demand for identifying and controlling toxic air contaminants in environmental justice communities, we have recently developed a cost-effective spark-induced breakdown spectroscopy (SIBS) instrument for detecting and quantifying toxic metal air pollutants. We characterized the detection limit and linearity of this SIBS instrument by analyzing nebulized elemental standard solutions. The experimental parameters affecting SIBS performance were optimized, including the time delay to observation, the distance between electrodes, and the ablation voltage. The instrument successfully detected Cr, Cu, Mn, Fe, Zn, Co, and Ni, with limits of detection ranged from 0.05 μg m^{-3} to 0.81 μg m^{-3} at a flow rate of 15 l min^{-1} and a 30 min sampling duration. Similar to other investigations using ion breakdown spectroscopy, we did not observe strong emissions lines for As, Sb, Se, Hg, Pb, and Cd, which were likely due to spectral overlap, matrix effects, and the limited detection range of the optical components. Overall, SIBS is a promising technique for field measurements of toxic metals for environmental justice, industrial and urban applications.

Keywords

Spark induced breakdown spectroscopy; Optical emission spectroscopy; Toxic metal

[*]Corresponding author. hynli@ucdavis.edu (H. Li).

[1]Now at California Air Resources Board, Sacramento, CA 95814, USA.

CRediT authorship contribution statement

Hanyang Li: Methodology, Formal analysis, Writing – original draft, experiments. **Leonardo Mazzei:** Writing – review & editing, experiments. **Christopher D. Wallis:** Methodology, Writing – review & editing. **Seyyed Ali Davari:** Methodology, Writing – review & editing. **Anthony S. Wexler:** Methodology, Investigation, Writing – review & editing, principal investigator.

Declaration of competing interest

The authors declare that they have no known competing financial interests or personal relationships that could have appeared to influence the work reported in this paper.

Appendix A. Supplementary data

Supplementary data to this article can be found online at https://doi.org/10.1016/j.atmosenv.2021.118666.

1. Introduction

The term “heavy metals” refers to metallic elements that have high density, atomic weight, or specific gravity (Duffus, 2002; Popoola et al., 2018; Suvarapu and Baek, 2017). They enter the atmosphere by both natural processes (e.g., off-gassing from the earth’s crust and weathering of rocks) and anthropogenic emissions from industrial and agricultural activities (Cheri and Tavassoli, 2011; Singh et al., 2011). Exposure to high concentrations of heavy metals may cause major health issues (Rehman et al., 2018). For example, inhalation of hexavalent chromium (Cr(VI)), cadmium (Cd), lead (Pb), mercury (Hg), and nickel (Ni) have been found to be associated with cancers of lung, liver, and kidney (Rahman and Singh, 2019). Some heavy metals such as copper (Cu), zinc (Zn), iron (Fe), manganese (Mn), and cobalt (Co) are required for metabolic activity at low concentrations, but can cause adverse health effect if exposed to high concentrations (Tchounwou et al., 2012). Consequently, identification and quantification of heavy metals in the atmosphere are necessary for occupational health and environmental justice concerns, and for developing air pollution management strategies.

Among the various techniques for monitoring heavy metals, *in situ* measurements with optical emission spectroscopy (including spark-induced breakdown spectroscopy (SIBS, also referred to as spark-induced plasma and spark emission spectroscopy (Walters, 1977, 1969)) and laser-induced breakdown spectroscopy (LIBS)) have shown great potential because of their relatively low cost and easy operation (e. g., (Anabitarte et al., 2012; Hahn and Lunden, 2000; Hunter et al., 2000; Kim et al., 2019; Srungaram et al., 2013)). Compared to conventional instruments used to analyze elemental compositions (such as X-ray fluorescence (XRF) and inductively coupled plasma mass spectrometry (ICP-MS)), optical emission spectroscopy is a relatively simple method, which does not require complex sample preparation (Fichet et al., 2006; Zhang et al., 2014). Although a recently-developed XRF instrument (Xact 625, Cooper Environmental Inc.) has been gained extensive attention in the field of pollution detection due to its relatively high time resolution (1 h or less) and low air flow (16.7 l min^{-1}), its operation still requires frequent calibration and blank assessment (Belis et al., 2019; Furger et al., 2017; Tremper et al., 2018). Furthermore, the equipment and maintenance costs (e.g., replacement of filters) of the instrument are rather considerable. In comparison, optical emission spectroscopy has been claimed to be more cost-effective, compact, and fast-acting (Doh et al., 2019; Sdvizhenskii et al., 2020).

Rapid progress in optical and electronic components, the understanding of the mechanism of plasma emission, as well as the development of quantitative models have made optical emission spectroscopy attractive for aerosol measurements in various environmental conditions. For example, many laboratory studies have applied optical emission spectroscopy to detect metal particles (such as sodium (Na), magnesium (Mg), calcium (Ca), aluminum (Al)) by nebulizing elemental standard solutions (e.g., LIBS: Gallou et al. (2011) and Kim et al. (2019); SIBS: Diwakar and Kulkarni (2012)). For field studies, optical emission spectroscopy was traditionally used to measure particles emitted from combustion processes (e.g., LIBS: Ottesen et al. (1989) and Zhang et al. (1995); SIBS: Hunter et al. (2000) and Fraser et al. (1999)); however, recent studies have extended its application to

monitor ambient particles (e.g., LIBS: (Carranza et al., 2001; Hettinger et al., 2006; Kwak et al., 2012; Lithgow et al., 2004); SIBS: Yang et al. (2020)).

Within the laboratory studies of SIBS used for aerosol analysis, Diwakar and Kulkarni (2012) recently proposed a coaxial electrode system to create an electrical field such that the charged aerosols can be directed to the tip of the cathode, followed by ablation and spectral analysis. Using this technique, this group of authors further investigated the analytical performance of different types of particles (L. Zheng et al., 2016a; Zheng et al., 2018a), measured the system collection efficiency (Zheng et al., 2017), and explored the dynamic of spark discharge (Zheng et al., 2018b).

Based on these promising results of the SIBS instrument, we most recently developed a similar system to analyze atmospheric heavy metal particles (Davari and Wexler, 2020). Our instrument does not employ the charge-and-collect scheme of Diwakar et al. (2012) and the related works, but instead only collects particles by impacting them onto the cathode. Our previous work has concentrated on the development of cost-effective instrument components (including the construction of the spark generation enclosure and the delay generator) and the application of a machine learning approach (i.e., least absolute shrinkage and selection operator (LASSO)) to optimize the quantification of heavy metal particles (including Cr, Cu, Ni, and Pb) (Davari and Wexler, 2020). By using a pipette to apply dilutions of the pre-mentioned metals to the surface of ground electrode, we have achieved detection limits in the range of 3.55–54.40 ng mass of the element on the electrode.

In this work, we added an aerosol inlet to the instrument enabling it to characterize heavy metal particles nebulized from elemental standard solutions (0.5–5 μg ml^{-1}, corresponding to mass concentrations from 3 to 30 μg m^{-3}). The spectral behaviors with respect to plasma parameters (i.e., delay time, breakdown voltage, and interelectrode distance) were investigated. Using the optimal plasma parameters, we then tested different heavy metals included by the US Environmental Protection Agency (EPA) in the Hazardous Air Pollutants (HAPs) list, including Cr, Cu, Mn, Ni, Pb, Co, Hg, Fe, Zn, Cd, selenium (Se), arsenic (As), and antimony (Sb) (EPA, 2017). Calibration curve and limit of detection (LOD) for the detectable elements were obtained using univariate calibration. The ultimate goal of this work is to measure the presence of toxic metals in total suspended particles (TSP) at a low cost, which will allow environmental justice communities to quickly identify and respond to emission events, and thereby minimize the impacts of heath hazardous incidents. However, if analysis of the inhalable fraction is desired, size-selective inlets (such as a PM2.5 or PM10 head) can be attached to our instrument.

2. Methods

2.1. Operation of the spark-induced breakdown spectroscopy

The principle of SIBS is the generation of a spark discharge between two high-voltage electrodes, which results in the formation of a high-temperature and short-lived plasma. The plasma atomizes and excites particles loaded onto the ground electrode (see Section 2.2 for more details about particle collection). As the plasma cools, the excited atoms and ions return to their ground states, causing the plasma to emit light with discrete spectral peaks.

The emitted light from the plasma is then collected by a spectrometer for analysis. As each element in the periodic table has unique spectral peaks (Ralchenko et al., 2006), we can determine the chemical composition of the analyzed samples. The intensity of the spectral peaks can be used to quantify the amount of each element in the sample via calibration approaches (Diwakar and Kulkarni, 2012; Zheng et al., 2018a).

Our SIBS system consisted of three components: spark generation, delay generator, and spectra collection. The key parameters of the three components are summarized in Table 1 and the detailed design can be found in Davari and Wexler (2020). In general, the instrument uses low-voltage electronics and an Arduino microcontroller to control charging and discharging of a high voltage capacitor. During the charging phase of operation, the mechanical relay first connects the circuit between the boost converter (high voltage output) and the capacitor (charge phase, ~5 s). During the discharge phase, the relay disconnects the boost converter and directs the charge on the capacitor to the electrodes creating an arc. A photodiode is used to detect the spark and transmit a trigger signal to the delay. After a specified time interval (a few microseconds, controlled by a digital potentiometer), the delay generator sends a trigger pulse to the spectrometer to initiate data acquisition (See Fig. S1 for the schematic of the delay generator). Once the discharge phase is completed, the circuit will start a new cycle of charging and discharging.

Although we used a design similar to that used by Diwakar and Kulkarni (2012) and Zheng et al. (2016a, b) to ablate particles on the flat tip of the cathode, our design varied from theirs in terms of particle collection. We did not apply the high voltage to electrodes when collecting particles but instead we simply used a nozzle for impaction. As seen in Fig. 1a and c, a 3D-printed nozzle held the anode and impacted aerosol particles onto the cathode. The nozzle and cathode were mounted on a frame that enabled an adjustable separation distance (a few millimeters).

2.2. Generation and collection of heavy metal particles

An illustration of the aerosol sampling system is shown in Fig. 1b. We used a nebulizer (MiniHEART, Westmed, Inc.) to generate metal particles from an aqueous solution of metal salts. The nebulizer was driven by filtered compressed air with a flow rate of 8 l min^{-1} and a pressure of 125 kPa, with a liquid consumption rate of 10 ml h^{-1}. The air stream from the nebulizer was dried to a relative humidity (RH) of ~50% using a diffusion dryer and then mixed with additional HEPA-filtered air. A vacuum pump downstream maintained a total flow rate of 15 l min^{-1}. During experiments, we used ball valves to direct flow to either the spark generation enclosure (i.e., aerosol sampling period) or the exhaust duct (i.e., SIBS operation period).

A metal enclosure (0.55 m (L) × 0.5 m (W) × 0.42 m (H)) was constructed to house all physical and electrical components. The enclosure was connected to building exhaust and operated at negative pressure to confine toxic aerosol. During each sampling period, air from the nebulizer and drier passed to the nozzle (see Fig. 1a). The diameter of the nozzle is 1 mm (same diameter as the cathode, but much greater than the diameter of the anode tip (50 μm)), which allows the particles to exit the nozzle and impact on the surface of the cathode (theoretical cut-off diameter (D_{50}) = 0.43 μm, see the Supplementary Materials for

the detailed calculation). After sampling for a known period of time, the valve connecting the air flow to the enclosure was closed, and the high voltage charge and discharge cycles were performed.

In addition to the SIBS analysis, the test particles were passed into an Aerodynamic Particle Sizer (APS) (model 3321, TSI Inc.) to analyze the particle size distribution over the range of 0.45–10 μm aerodynamic diameter. Moreover, we calculated the mass concentration of the tested metal in the air (C_{air}, μg m^{-3}) using the following equation:

$$\mathbf{C_{air} = \frac{C_s \times solution\ consumption\ rate}{carrier\ gas\ flow\ rate}} \quad (1)$$

where C_s is the concentration of the metal solution (μg ml^{-1}), the solution consumption rate is in ml hr^{-1}, and the carrier gas flow rate is in m^3 hr^{-1}.

Similarly, the delivered mass of the tested metals by the nebulizer (M_d, μg) can be calculated as:

$$\mathbf{M_d = C_s \times solution\ consumption\ rate \times sampling\ duration} \quad (2)$$

M_d represents the total mass of particles transported in the air sampling system, and thus does not take into account particle wall losses and impaction efficiency through the nozzle. Theoretically, the impaction efficiency can be estimated based on the calculated Reynolds number and Stokes number of the tested particles (Rader and Marple, 1985). However, because we impacted particles onto a small deposition area as opposed to a flat surface, the impaction efficiency of our instrument will likely be smaller. With an overall capture efficiency of the collection electrode, M_d can be further converted to the deposited mass of the tested particles. Zheng et al. (2017) has conducted rigorous experiments to characterize the collection efficiency on probes as functions of particle size and probe geometries. At a given air flow rate (e.g., 5 l min^{-1}), the collection efficiency was found to increase from ~5% to 65% when the cathode diameter increased from 0.5 to 1.5 mm, but relatively independent of particle sizes within 1 μm. Because it remains uncertain how the collection efficiency of our instrument compares to that reported in Zheng et al. (2017), we simply use M_d to generate the calibration curves and calculate elemental LODs in this work.

2.3. Heavy metals

We tested thirteen heavy metals included on the EPA HAPs list, including Cr, Cu, Mn, Ni, Pb, Co, As, Sb, Hg, Fe, Zn, Se, and Cd (Table 2). Different concentrations of metal solution were prepared by diluting standard elemental solution (1000 μg ml^{-1}, AccuStandard Inc.) with deionized water. Table 2 also shows the atomic lines and LODs reported by previous studies for each investigated metal. To narrow the scope, we focused on the studies using aerosols nebulized from aqueous solutions. Using optical emission spectroscopy, Zhang et al. (1999) and Zheng et al. (2018a) found that different heavy metals can have very different

LODs, where Sb, As, Hg, Cd, and Pb tend to have greater LODs than the others. Because of differences in sampling time and flow rates, care should be taken when comparing LODs in μg m^{-3} across studies.

2.4. Spectra baseline correction

It has been acknowledged that baseline drift can significantly affect the robustness of spectrum analysis (Cai et al., 2018; Kuzmiakova et al., 2016; Lieber and Mahadevan-Jansen, 2003). In our experiments, the integration time used for spectral acquisition (3 ms, Table 1) was much longer than the lifetime of spark plasma (~20 μs, Fig. 2), so the background noise of the spectra is needed to remove before analysis. In the present work, we conducted a simple automatic baseline correction to separate signal response to analytes from interference effects of the anode and cathode spectra and background noise. Specifically, we first applied K-means clustering (K = 5) to the original spectrum detected by the spectrometer (Kanungo et al., 2002; Verbeeck et al., 2020). The spectrum is grouped into K clusters based on the similarity of intensity values. Each cluster has a centroid which is the mean of the intensities that comprise the cluster. Then the group that has the lowest cluster center is selected since the data in this group are closest to the baseline. We next performed the Chebyshev polynomial fitting to the selected data and derived the baseline of the spectrum (Smyth, 2014). The detailed results of K-means clustering analysis and the Chebyshev polynomial fitting are provided in the Supplementary Materials, and an example of a spectrum and its corresponding baseline is shown in Fig. S2. Finally, the original spectrum is divided by the baseline to obtain a baseline-corrected spectrum (hereafter referred to as “relative intensity”).

3. Results

3.1. Spark plasma characteristics

To optimize the spark ignition condition for spectral analysis, we investigated the behaviors of the plasma under different spark characteristics, including delay time, spark voltage, and interelectrode distance (Srungaram et al., 2013; Zheng et al., 2016b). We carried out the experiments by generating spark discharges in the absence of and in the presence heavy metal particles on the cathode and collecting the spectra after each individual spark. The results were evaluated by comparing the intensity of spectral lines emitted from the electrodes (tungsten, W) and analyte with respect to the change in spark characteristics. Fig. S3 compares the W emission lines detected by our SIBS instrument to NIST atomic spectra database.

3.1.1. Influence of the delay time—The early stage of plasma evolution is dominated by continuum radiation, which can hide the emission lines related to the chemical species of interest (Anabitarte et al., 2012). However, because continuum radiation decays faster than the elemental emission lines, we can select a proper delay time to detect elements. Fig. 2a shows a set of spectra with different delay times and Fig. 2b and c shows the representative emission lines of W at 304.52, 429.77, and 522.43 nm as a function of delay time. For each delay time, ten spectra were recorded and the average spectrum was calculated. As seen in the figure, the spectral intensities decrease with increasing delay time, suggesting a

lifetime of ~20 μs. In addition to W emission lines, the studied delay times exhibit similar results for the analytes of interest. For example, by changing the delay times when ablating Cr particles, we found that the relative intensities of Cr have a clear maximum at a delay time of ~2 μs (Fig. S4a). After baseline correction, we set the delay time to be 1.88 μs for subsequent experiments since this value yields the strongest relative intensities of W and analyte.

3.1.2. Influence of the applied voltage—Theoretically, increasing the applied voltage could create a stronger microdischarge between electrodes, and therefore excite more energetic electrons and ions in the plasma (Jahanmiri et al., 2012; Zheng et al., 2016a, b). By changing the applied voltage from 4,500 V to ~10,000 V, we observed that the spectral intensities of W increase continuously (Fig. S5a). However, the baseline correction of the spectra removes the pronounced trend related to voltage changing (Fig. 3a for the W results and Fig. S4b for the analyte results). In subsequent experiments, a voltage of 6,000 V is selected.

3.1.3. Influence of the distance between electrodes—We next tested different interelectrode distances to find the optimal condition for elemental analysis. Theoretically, the interelectrode distance should be neither too short to avoid generations of a weak plasma, nor too long to ensure the consistency and stability of the spark path (Doh et al., 2019; Jung et al., 2020). Besides the influence on the generated spark plasma, the interelectrode distance also affects the distance between the nozzle and impaction plate because the anode was mounted to the nozzle (Fig. 1a). To achieve an ideal particle collection efficiency, the impactor should be designed so that the nozzle-to-plate distance is not much greater than the nozzle outlet diameter (Marple and Willeke, 1976). We therefore varied the interelectrode distance from 1 to 2 mm with a step size of 0.25 mm (corresponding to a nozzle-to-plate distance of 2.5–3.5 mm), and studied both W and analyte signals.

As shown in Figs. 3b and S5b, different W emission lines exhibit slightly different patterns with respect to the interelectrode distance. W emission lines at 429.77 and 522.43 nm show an initial increase with the interelectrode distance, reaching a peak at 1.5 mm followed by a decrease; whereas, the W emission line at 304.52 nm remains stable for all interelectrode distances. We also obtained the spectra for ablation of Cr particles collected on the cathode and showed the results in Fig. S4c. Similar to the W results, changing interelectrode distance did not result in significant changes in the emission signal of Cr. Moreover, there is no similar relationship between spectral intensities and electrode distances for the two strong Cr emission lines.

Although we only studied a relatively small, but practical, range of electrode distance, within this range its influence on the emission signals appears to be mild. In this work we designed the interelectrode distance to be 1.5 mm in this work, which results in a nozzle-to-plate distance of 3 mm (three times the nozzle diameter).

3.2. Detection of heavy metal particles

In order to minimize carryover of residual particle depositions from one experiment to another, we performed multiple ablations after each particle deposition period. Our results

demonstrate that one or multiple sparks are required to ablate different masses of deposited particles on the cathode. For example, a single ablation is sufficient to clean off a low mass loading on the cathode (e.g., 1 μg ml^{-1} solution and 1 min sampling duration for a loading of Cr particles), while multiple ablations are needed for high mass loadings (e.g., 4 sparks are required for an experiment using 2 μg ml^{-1} solution and 5 min sampling duration for a loading of Cr particles). Furthermore, the required number of ablations varies with metal species. To capture the entire signals of analyte from different number of sparks and compare across experiments, we summed the spectral response of five consecutive sparks after each particle loading (similar to Diwakar and Kulkarni (2012) and Zheng and Kulkarni (2017)). Hereafter, if not specified, the spectrum is the summed spectrum of five sparks from each experiment.

Using the current SIBS setup, we successfully detected 7 of 13 heavy metals, including Cr, Cu, Mn, Fe, Zn, Co, and Ni (see Section 4.2 for our speculations on the metals which were not detected). Besides the investigated heavy metals, we also observed the emissions lines of Na and Ca due to impurities in the nebulizing water. Fig. 4 shows an example of our SIBS results for Cr. The experiments were conducted using an aqueous solution of $Cr(NO_3)_3$ with a concentration of 2 μg ml^{-1} (corresponding to 12.5 μg m^{-3} of Cr in the air, calculated by Eq. (1)). By varying sampling durations from 0.5 to 5 min, we varied the mass of Cr particles loaded on the ground electrode. Each experiment was repeated at least three times to assess for consistency of results. As seen in Fig. 4, longer sampling duration yields greater spectral intensity and different Cr emission lines can be easily detected (with the strongest one at 520.6 nm). When comparing the two panels of Fig. 4, it is clear that our baseline correction method eliminates the background shift due to the change of particle loading and results in similar relative intensities at all wavelengths except for the emission lines produced by Cr, Na, and Ca.

3.3. Aerosol mass concentration

The APS measurements of particle size distributions demonstrate that the tested heavy metals have a single mode with a geometric mean diameter (D_p) of ~0.55 μm (Fig. 5a). Increasing solution concentration increases D_p, although the effect is weak (e.g., from 0.53 μm (1 μg ml^{-1}) to 0.62 μm (5 μg ml^{-1}) for Co particles). Comparing the total mass concentration derived by the APS to C_{air} calculated by Eq. (1), we found very small discrepancies between the APS results and C_{air} for the solution concentrations of 2 and 5 μg ml^{-1}; however, lower solution concentrations (e.g., 0.5 and 1 μg ml^{-1}) can yield large discrepancies between the APS results and C_{air} (Fig. 5b). The large discrepancies are not surprising. The location of the distribution mode is near the lower boundary of the APS range (0.45 μm, Fig. S7), so the APS appears to miss the quantification of small particles generated by aqueous solutions of low concentrations. Nevertheless, the relatively good agreement for the solution concentrations of 2 and 5 μg ml^{-1} implies a minimal particle loss during transport between nebulization and measurement in APS.

4. Discussion

4.1. Calibration and limit of detection

Greater particle concentration and longer sampling duration should both result in more particles loaded on the electrode, so we first explore their effects on the SIBS signal. Fig. 6a shows the relative intensity of Cr at 520.6 nm as a function of solution concentration, with different sampling durations. As seen in the figure, the signal of Cr increases gradually with the increase of solution concentration. Moreover, longer durations can also lead to stronger signal of Cr under certain conditions of solution concentration. Eq. (2) implies that different combinations of sampling duration and solution concentration can yield same the M_d (e.g., 0.5 μg ml^{-1} × 2 min and 1 μg ml^{-1} × 1 min), which is anticipated to result in the same SIBS signals. Fig. 6b confirms our expectation that the SIBS signal is only proportional to the actual mass of the delivered particles through the air sampling system, regardless of the sampling duration and solution concentration used to generate particles. This leads us to believe that the ablation efficiency of our instrument remain constant within the mass loading tested in the present work. Therefore, our instrument should be applicable to studies of heavy metals from environments with different levels of contamination by changing sampling durations.

We next construct calibration curves for all tested metals (Fig. 7a and Table 3). For each element, the relative intensity of one representative emission line is plotted against the delivered mass (M_d in Eq. (2)) and "air concentration (C_{air} in Eq. (1)) × sampling duration" on a linear scale. The representative emission lines were picked based on the criteria of high intensity of atomic spectral lines in the detected wavelength range (250–800 nm) and low interference with other elements (e. g., W, Ca, and Na emission lines). Fig. 7a suggests that the sensitivity of our SIBS instrument to different mass loading varies with metal types. For example, Cr has the largest calibration curve slope indicating that our instrument is most sensitive to Cr particles. In comparison, our instrument is much less sensitive to mass changes of Ni and Zn.

The LODs of the metals can be determined based on the standard deviation of the response (σ) and the slope of the calibration curve (S):

$$\mathbf{LOD} = 3.33\boldsymbol{\sigma} / \mathbf{S} \quad (3)$$

where σ is derived using the results of 20 sparks in the absence of heavy metal particles. Using the calibration curves in Fig. 7a, we computed the LODs in terms of the delivered particle mass, which ranged from 0.03 to 0.36 μg (Table 3). LODs in terms elemental air concentrations (μg m^{-3}) can be obtained by assuming a sampling duration and an air flow rate. Using the current sampling system at a flow rate of 15 l min^{-1}, the LODs of our instrument is estimated to range from 0.14 μg m^{-3} for Cr to 2.42 μg m^{-3} for Ni (10-min sampling), and from 0.05 μg m^{-3} for Cr to 0.81 μg m^{-3} for Ni (30-min sampling). The LODs estimated at other sampling intervals can be found in Fig. 7b. We further verify the reasonability of the LODs by conduction experiments using aqueous solutions with

concentrations at the limit of quantification (LOQ, defined as 3 times LOD). The results were evaluated in Fig. S8 by comparing the analyte spectral intensities at the corresponding LOQs and the intensities of blank samples. The existence of peaks was verified and no background disturbance was observed, confirming the robustness of the calculated LODs.

Although it is not fair to directly compare the LODs obtained in the present work to the results reported in the previous LIBS/SIBS studies due to the differences in plasma characteristics, selected emission lines, and nozzle aerosol deposition characteristics, it is worthwhile to evaluate our detection efficiencies for different metals using the other studies. Our instrument was able to detect most of the metals that Zhang et al. (1999) and Zheng et al. (2018) determined to have LODs less than 1 μg m^{-3} (Table 2). Our study did not cover extreme concentrations necessary to detect high LOD metals (e.g., Hg with a LOD of 680 μg m^{-3} and As with a LOD of 600 μg m^{-3}) since such high air concentrations do not occur outside of extreme occupational and industrial environments. Moreover, consistent with these two studies and other works (e.g., (Diwakar et al., 2012; Gravel et al., 2011; Panne et al., 2001)), we observed that the optical emission spectroscopy is more sensitive to certain heavy elements yielding lower LODs for elements such as Cr, Cu, and Mn.

4.2. Thoughts on instrument capabilities

There are several caveats when using the current experimental setup to analyze heavy metal particles. First, the particle sizes of the elements are relatively small (0.55–0.6 μm, see Fig. 5a), so it remains uncertain about the performance of our SIBS instrument for large particles (e.g., coarse particles). For example, previous studies have shown that the signal strength of LIBS/SIBS tends to be reduced for large particles. Gallou et al. (2011) reported an abrupt deviation of Cu emission signal when testing particles greater than 7 μm. Similarly, Yang et al. (2020) found that large particles (e.g., PM10) can disrupt the breakdown medium and decrease the signal of LIBS and SIBS. Furthermore, the variation of collection efficiency as a function of particle sizes is worth investigation to derived LODs in terms of the deposited mass of particles. It is also crucial to understand at what concentration the calibration curves deviate from linearity and if different toxic metals have similar nonlinear effects at high particle loadings.

Second, a number of W emission lines from the material of electrodes may interfere with the detection of some metals. In the present work, the detection of Pb particles at 405.78 nm was hidden by the strong emission lines of W at 404.4 and 407.39 nm (forming a “shoulder” which spans 405.5 nm). This shoulder overlaps the Pb emission line and constrains us to draw general conclusions about Pb detection. An alternative is to use platinum or iridium electrodes, as they do not have strong emission lines around 405 nm.

Third, the light detection range of the spectrometer and optical fiber appears to prevent us from detecting some metals. As seen in Table 2, the strong emission lines of As, Se, and Sb are beyond the lower detection range of our optical fiber (250 nm), so we are not able to detect them using the current setup.

Lastly, spectral matrix effects may limit the utility of our instrument for quantitative analysis of heavy metals in the present work. Many studies have reported that matrix effects can

result in large uncertainties when using univariate calibration, and therefore proposed various multivariate calibration methods for elemental determination (e.g., (Debus et al., 2019; Takahama et al., 2019; Zheng et al., 2018a)). Although the intensity at 405.78 nm does not allow us to derive a univariate calibration curve of Pb in the present work, our previous study (Davari and Wexler, 2020) successfully built a LASSO model (similar to multivariate calibration) for the quantification of Pb and demonstrated a reasonable R^2 of 0.9.

5. Conclusions

In this work, we modified our recently-developed SIBS system to detect heavy metal particles nebulized from aqueous solutions. The major plasma characteristics that affect the analytical performance have been optimized for the best identification and quantification. Using a delay time of 1.88 μs, a voltage of 6000 V, and an interelectrode distance of 1.55 mm, the system effectively detects multiple metals (including Cr, Cu, Mn, Fe, Zn, Co, and Ni) and implies good reproducibility of analyte signal. We applied the univariate calibration method to determine LODs of the metals in terms of both delivered mass and air concentration. The tested metals exhibit a broad range of LODs, varying from 0.14 μg m^{-3} (Cr) to 2.42 μg m^{-3} (Ni) at a flow rate of 15 l min^{-1} for a 10 min sampling duration. Heavy metals of As, Sb, Se, Hg, Pb, and Cd cannot be identified using the current experimental setup, and we suspect that it may be due to the interference of atomic lines of W electrodes, spectral matrix effects, and the limited wavelength range of our optical components (as discussed in Section 4.2). Future work will be conducted to improve the instrument for the detection of these metals.

Certainly, the proposed low-cost SIBS system is a promising instrument for *in situ* analysis of heavy metal particles and/or any elements of interest. Considering the LODs of our instrument, it may be more applicable to industrial and polluted urban environments. Mamun et al. (2019) recently reviewed the field studies of heavy metals around the world and found that the concentration of toxic metals is typically less than 100 ng m^{-3}, but with large variation (e.g., the concentration of Zn ranges from 1 to 340 ng m^{-3} in North America). In addition, Zn and Pb, respectively, have the highest and lowest concentration among the toxic metals. The authors also reported large variation in the sizes of toxic metals due to complicated sources and influence of meteorological conditions. However, most of the anthropogenic toxic metals (such as Zn, Ni, Cd, and Pb) are concentrated in the fine range (<2.5 μm).

To apply our instrument to environments with relatively low metal concentrations, possible adjustments include increasing sampling flow rate and sampling duration. For example, using a sampling duration of 30 min, the LOD of Ni (the least sensitive element detected by our instrument) is expected to be reduced to 0.81 μg m^{-3}. However, in practice, the use of our instrument faces a trade-off between cost and performance. Using a large pump means a cost of power and weight; similarly, longer sampling period means a cost in temporal resolution.

However, our characterization of the instrument is not without limitation. As the preliminary study towards the use of our SIBS instrument, our goal is not to give a precise report of LODs and measurement uncertainty of the instrument, but to provide a scheme to semi-quantitatively measure atmospheric particles. Hence, we limited our calibration to nebulized particles with a geometric mean diameter of ~0.6 μm and probed the approximate LOD with respect to different collection times. Further work will be undertaken to compare the performance of our instrument against traditional elemental analytical techniques for the analysis of particles with different sizes and/or from different pollution sources. Further efforts will also focus on the characterization of the collection efficiency and overall instrument sensitivity.

Supplementary Material

Refer to Web version on PubMed Central for supplementary material.

Funding

This research has been funded by the California Air Resources Board, contract 17RD022. We would like to thank Dr. Pramod Kulkarni and an anonymous reviewer for their valuable suggestions that have improved this manuscript.

References

Anabitarte F, Cobo A, Lopez-Higuera JM, 2012. Laser-induced breakdown spectroscopy: fundamentals, applications, and challenges. ISRN Spectrosc 2012, 1–12. 10.5402/2012/285240.

Belis CA, Pikridas M, Lucarelli F, Petralia E, Cavalli F, Calzolai G, Berico M, Sciare J, 2019. Source apportionment of fine PM by combining high time resolution organic and inorganic chemical composition datasets. Atmos. Environ. X 3, 100046. 10.1016/j.aeaoa.2019.100046.

Cai Y, Yang C, Xu D, Gui W, 2018. Baseline correction for Raman spectra using penalized spline smoothing based on vector transformation. Anal. Methods 10, 3525–3533. 10.1039/C8AY00914G.

Carranza JE, Fisher BT, Yoder GD, Hahn DW, 2001. On-line analysis of ambient air aerosols using laser-induced breakdown spectroscopy. Spectrochim. Acta Part B At. Spectrosc 56, 851–864. 10.1016/S0584-8547(01)00183-5.

Cheri MS, Tavassoli SH, 2011. Quantitative analysis of toxic metals lead and cadmium in water jet by laser-induced breakdown spectroscopy. Appl. Opt 50, 1227. 10.1364/AO.50.001227. [PubMed: 21460994]

Davari SA, Wexler AS, 2020. Quantification of toxic metals using machine learning techniques and spark emission spectroscopy. Atmos. Meas. Tech 13, 5369–5377. 10.5194/amt-13-5369-2020. [PubMed: 38596355]

Debus B, Takahama S, Weakley AT, Seibert K, Dillner AM, 2019. Long-term strategy for assessing carbonaceous particulate matter concentrations from multiple fourier transform infrared (FT-IR) instruments: influence of spectral dissimilarities on multivariate calibration performance. Appl. Spectrosc 73, 271–283. 10.1177/0003702818804574. [PubMed: 30223670]

Diwakar P, Kulkarni P, Birch ME, 2012. New approach for near-real-time measurement of elemental composition of aerosol using laser-induced breakdown spectroscopy. Aerosol Sci. Technol 46, 316–332. 10.1080/02786826.2011.625059. [PubMed: 26692632]

Diwakar PK, Kulkarni P, 2012. Measurement of elemental concentration of aerosols using spark emission spectroscopy. J. Anal. At. Spectrom 27, 1101. 10.1039/c2ja30025g. [PubMed: 26491209]

Doh I-J, Gondhalekar C, Patsekin V, Rajwa B, Hernandez K, Bae E, Paul Robinson J, 2019. A portable spark-induced breakdown spectroscopic (SIBS) instrument and its analytical performance. Appl. Spectrosc 73, 698–708. 10.1177/0003702819844792. [PubMed: 30990055]

Duffus JH, 2002. “Heavy metals” a meaningless term? (IUPAC Technical Report). Pure Appl. Chem 74, 793–807. 10.1351/pac200274050793.

EPA, 2017. Initial list of hazardous air pollutants with modifications. US Environ. Prot. Agency [WWW Document] https://www.epa.gov/haps/initial-list-hazardous-air-pollutants-modifications.

Fichet P, Tabarant M, Salle B, Gautier C, 2006. Comparisons between LIBS and ICP/OES. Anal. Bioanal. Chem 385, 338–344. 10.1007/s00216-006-0384-7. [PubMed: 16609842]

Fraser ME, Hunter AJ, Davis SJ, 1999. Real-time monitoring of airborne metals. Environ. Monit. Remediat. Technol 3534, 262–270. 10.1117/12.339004.

Furger M, Minguillón MC, Yadav V, Slowik JG, Hüglin C, Fröhlich R, Petterson K, Baltensperger U, Prévôt ASH, 2017. Elemental composition of ambient aerosols measured with high temporal resolution using an online XRF spectrometer. Atmos. Meas. Tech 10, 2061–2076. 10.5194/amt-10-2061-2017.

Gallou G, Sirven JB, Dutouquet C, Le Bihan O, Frejafon E, 2011. Aerosols analysis by LIBS for monitoring of air pollution by industrial sources. Aerosol Sci. Technol 45, 918–926. 10.1080/02786826.2011.566899.

Gravel J-FY, Doucet FR, Bouchard P, Sabsabi M, 2011. Evaluation of a compact high power pulsed fiber laser source for laser-induced breakdown spectroscopy. J. Anal. At. Spectrom 26, 1354. 10.1039/c0ja00228c.

Hahn DW, Lunden MM, 2000. Detection and analysis of aerosol particles by laser-induced breakdown spectroscopy. Aerosol Sci. Technol 33, 30–48. 10.1080/027868200410831.

Hettinger B, Hohreiter V, Swingle M, Hahn DW, 2006. Laser-induced breakdown spectroscopy for ambient air particulate monitoring: correlation of total and speciated aerosol particle counts. Appl. Spectrosc 60, 237–245. 10.1366/000370206776342544. [PubMed: 16608565]

Hunter AJR, Davis SJ, Piper LG, Holtzclaw KW, Fraser ME, 2000. Spark-induced breakdown spectroscopy: a new technique for monitoring heavy metals. Appl. Spectrosc 54, 575–582. 10.1366/0003702001949753.

Jahanmiri A, Rahimpour MR, Mohamadzadeh Shirazi M, Hooshmand N, Taghvaei H, 2012. Naphtha cracking through a pulsed DBD plasma reactor: Effect of applied voltage, pulse repetition frequency and electrode material. Chem. Eng. J 191, 416–425. 10.1016/j.cej.2012.02.031.

Jung J, Yang J-H, Yoh JJ, 2020. An optimal configuration for spark-induced breakdown spectroscopy of bulk minerals aimed at planetary analysis. J. Anal. At. Spectrom 35, 1103–1114. 10.1039/D0JA00057D.

Kanungo T, Mount DM, Netanyahu NS, Piatko CD, Silverman R, Wu AY, 2002. An efficient k-means clustering algorithm: analysis and implementation. IEEE Trans. Pattern Anal. Mach. Intell 24, 881–892. 10.1109/TPAMI.2002.1017616.

Kim G, Kim K, Maeng H, Lee H, Park K, 2019. Development of aerosol-LIBS (laser induced breakdown spectroscopy) for real-time monitoring of process-induced particles. Aerosol Air Qual. Res 19, 455–460. 10.4209/aaqr.2018.08.0312.

Kuzmiakova A, Dillner AM, Takahama S, 2016. An automated baseline correction protocol for infrared spectra of atmospheric aerosols collected on polytetrafluoroethylene (Teflon) filters. Atmos. Meas. Tech 9, 2615–2631. 10.5194/amt-9-2615-2016.

Kwak J-H, Kim G, Kim Y-J, Park K, 2012. Determination of heavy metal distribution in PM 10 during Asian dust and local pollution events using laser induced breakdown spectroscopy (LIBS). Aerosol Sci. Technol 46, 1079–1089. 10.1080/02786826.2012.692492.

Lieber CA, Mahadevan-Jansen A, 2003. Automated method for subtraction of fluorescence from biological Raman spectra. Appl. Spectrosc 57, 1363–1367. 10.1366/000370203322554518. [PubMed: 14658149]

Lithgow GA, Robinson AL, Buckley SG, 2004. Ambient measurements of metal-containing PM2.5 in an urban environment using laser-induced breakdown spectroscopy. Atmos. Environ 38, 3319–3328. 10.1016/j.atmosenv.2004.03.017.

Al Mamun A, Cheng I, Zhang L, Dabek-Zlotorzynska E, Charland J-P, 2019. Overview of size distribution, concentration, and dry deposition of airborne particulate elements measured worldwide. Environ. Rev 1–12 10.1139/er-2019-0035.

Marple VA, Willeke K, 1976. Impactor design. Atmos. Environ 10, 891–896. 10.1016/0004-6981(76)90144-X.

Ottesen DK, Wang JCF, Radziemski LJ, 1989. Real-time laser spark spectroscopy of particulates in combustion environments. Appl. Spectrosc 43, 967–976. 10.1366/0003702894203778.

Panne U, Neuhauser RE, Theisen M, Fink H, Niessner R, 2001. Analysis of heavy metal aerosols on filters by laser-induced plasma spectroscopy. Spectrochim. Acta Part B At. Spectrosc 56, 839–850. 10.1016/S0584-8547(01)00209-9.

Popoola LT, Adebanjo SA, Adeoye BK, 2018. Assessment of atmospheric particulate matter and heavy metals: a critical review. Int. J. Environ. Sci. Technol 15, 935–948. 10.1007/s13762-017-1454-4.

Rader DJ, Marple VA, 1985. Effect of ultra-stokesian drag and particle interception on impaction characteristics. Aerosol Sci. Technol 4, 141–156. 10.1080/02786828508959044.

Rahman Z, Singh VP, 2019. The relative impact of toxic heavy metals (THMs) (arsenic (As), cadmium (Cd), chromium (Cr)(VI), mercury (Hg), and lead (Pb)) on the total environment: an overview. Environ. Monit. Assess 191, 419. 10.1007/s10661-019-7528-7. [PubMed: 31177337]

Ralchenko Y, Jou FC, Kelleher DE, Kramida A, Musgrove A, Reader J, Wiese WL, Olsen KJ, 2006. Nist Atomic Spectra Database, version 3.1. 0.

Rehman K, Fatima F, Waheed I, Akash MSH, 2018. Prevalence of exposure of heavy metals and their impact on health consequences. J. Cell. Biochem 119, 157–184. 10.1002/jcb.26234. [PubMed: 28643849]

Sdvizhenskii PA, Lednev VN, Asyutin RD, Grishin MY, Tretyakov RS, Pershin SM, 2020. Online laser-induced breakdown spectroscopy for metal-particle powder flow analysis during additive manufacturing. J. Anal. At. Spectrom 35, 246–253. 10.1039/C9JA00343F.

Singh R, Gautam N, Mishra A, Gupta R, 2011. Heavy metals and living systems: an overview. Indian J. Pharmacol 43, 246. 10.4103/0253-7613.81505. [PubMed: 21713085]

Smyth GK, 2014. Polynomial approximation. In: Wiley StatsRef: Statistics Reference Online. John Wiley & Sons, Ltd, Chichester, UK. 10.1002/9781118445112.stat05031.

Srungaram PK, Ayyalasomayajula KK, Yu-Yueh F, Singh JP, 2013. Comparison of laser induced breakdown spectroscopy and spark induced breakdown spectroscopy for determination of mercury in soils. Spectrochim. Acta Part B At. Spectrosc 87, 108–113. 10.1016/j.sab.2013.05.009.

Suvarapu LN, Baek S-O, 2017. Determination of heavy metals in the ambient atmosphere. Toxicol. Ind. Health 33, 79–96. 10.1177/0748233716654827. [PubMed: 27340261]

Takahama S, Dillner AM, Weakley AT, Reggente M, Bürki C, Lbadaoui-Darvas M, Debus B, Kuzmiakova A, Wexler AS, 2019. Atmospheric particulate matter characterization by Fourier transform infrared spectroscopy: a review of statistical calibration strategies for carbonaceous aerosol quantification in US measurement networks. Atmos. Meas. Tech 12, 525–567. 10.5194/amt-12-525-2019.

Tchounwou PB, Yedjou CG, Patlolla AK, Sutton DJ, 2012. Heavy Metal Toxicity and the Environment. 10.1007/978-3-7643-8340-4_6, 133–164.

Tremper AH, Font A, Priestman M, Hamad SH, Chung T-C, Pribadi A, Brown RJC, Goddard SL, Grassineau N, Petterson K, Kelly FJ, Green DC, 2018. Field and laboratory evaluation of a high time resolution x-ray fluorescence instrument for determining the elemental composition of ambient aerosols. Atmos. Meas. Tech 11, 3541–3557. 10.5194/amt-11-3541-2018.

Verbeeck N, Caprioli RM, Van de Plas R, 2020. Unsupervised machine learning for exploratory data analysis in imaging mass spectrometry. Mass Spectrom. Rev 39, 245–291. 10.1002/mas.21602. [PubMed: 31602691]

Walters JP, 1977. Spark discharge: application multielement spectrochemical analysis. Science 80 (198), 787–797. 10.1126/science.198.4319.787.

Walters JP, 1969. Historical Advances in spark emission spectroscopy. Appl. Spectrosc 23 (4), 317–331.

Yang J-H, Jung J, Ryu J-H, Yoh JJ, 2020. Real-time monitoring of toxic components from fine dust air pollutant samples by utilizing spark-induced plasma spectroscopy. Chemosphere 257, 127237. 10.1016/j.chemosphere.2020.127237. [PubMed: 32512334]

Zhang H, Singh JP, Yueh F-Y, Cook RL, 1995. Laser-induced breakdown spectra in a coal-fired MHD facility. Appl. Spectrosc 49, 1617–1623. 10.1366/0003702953965759.

Zhang H, Yueh F-Y, Singh JP, 1999. Laser-induced breakdown spectrometry as a multimetal continuous-emission monitor. Appl. Opt 38, 1459. 10.1364/AO.38.001459. [PubMed: 18305767]

Zhang Y, Jia Y, Chen J, Shen X, Liu Y, Zhao L, Li D, Han P, Xiao Z, Ma H, 2014. Comparison of the analytical performances of laser-induced breakdown spectroscopy and spark-OES. ISIJ Int. 54, 136–140. 10.2355/isijinternational.54.136.

Zheng L, Kulkarni P, 2017. Rapid elemental analysis of aerosols using atmospheric glow discharge optical emission spectroscopy. Anal. Chem 89, 6551–6558. 10.1021/acs.analchem.7b00691. [PubMed: 28513144]

Zheng L, Kulkarni P, Birch ME, Deye G, Dionysiou DD, 2016a. Near real-time measurement of carbonaceous aerosol using microplasma spectroscopy: application to measurement of carbon nanomaterials. Aerosol Sci. Technol 50, 1155–1166. 10.1080/02786826.2016.1224804. [PubMed: 28638174]

Zheng L, Kulkarni P, Dionysiou DD, 2018a. Calibration approaches for the measurement of aerosol multielemental concentration using spark emission spectroscopy. J. Anal. At. Spectrom 33, 404–412. 10.1039/C7JA00252A. [PubMed: 35673324]

Zheng L, Kulkarni P, Diwakar P, 2018b. Spatial and temporal dynamics of a pulsed spark microplasma used for aerosol analysis. Spectrochim. Acta Part B At. Spectrosc 144, 55–62. 10.1016/j.sab.2018.03.008.

Zheng L, Kulkarni P, Zavvos K, Liang H, Birch ME, Dionysiou DD, 2017. Characterization of an aerosol microconcentrator for analysis using microscale optical spectroscopies. J. Aerosol Sci 104, 66–78. 10.1016/j.jaerosci.2016.11.007. [PubMed: 28626243]

Zheng P, Chen Y, Wang J, Xue S, 2016b. A pulsed atmospheric-pressure discharge generated in contact with flowing electrolyte solutions for metal element analysis by optical emission spectrometry. J. Anal. At. Spectrom 31, 2037–2044. 10.1039/C6JA00213G.

HIGHLIGHTS

- We developed an inexpensive SIBS instrument for detecting toxic metal pollutants.
- The experimental parameters affecting SIBS performance were optimized.
- The instrument successfully detected Cr, Cu, Mn, Fe, Zn, Co, and Ni.
- We used univariate calibration to obtain detection limits (0.05–0.81 μg m^{-3}).

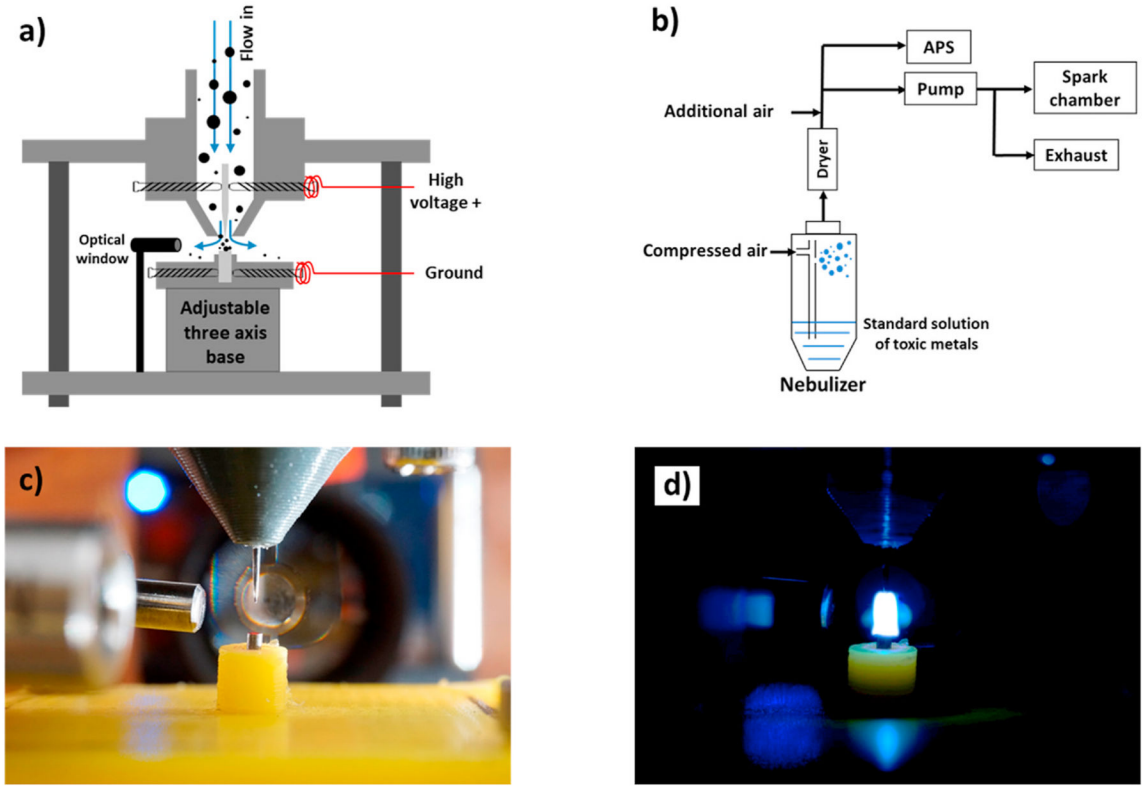

Fig. 1.

Construction of the SIBS system and air sampling system: (a) schematic diagram of the nozzle and electrode assembly (not to scale), (b) schematic diagram of the aerosol collection setup, (c) photograph of the electrodes (foreground), optical fiber communicating with the delay generator (left of the electrodes) and the lens communicated with the spectrometer (behind the electrodes), and (d) photograph of an arc generated between the electrodes. To better illustrate the arc, the photographs shown in panels c) and d) were taken with a nozzle-to-plate distance of 7 mm (greater than the final nozzle-to-plate distance used in the study, see Section 3.1.3 for more details).

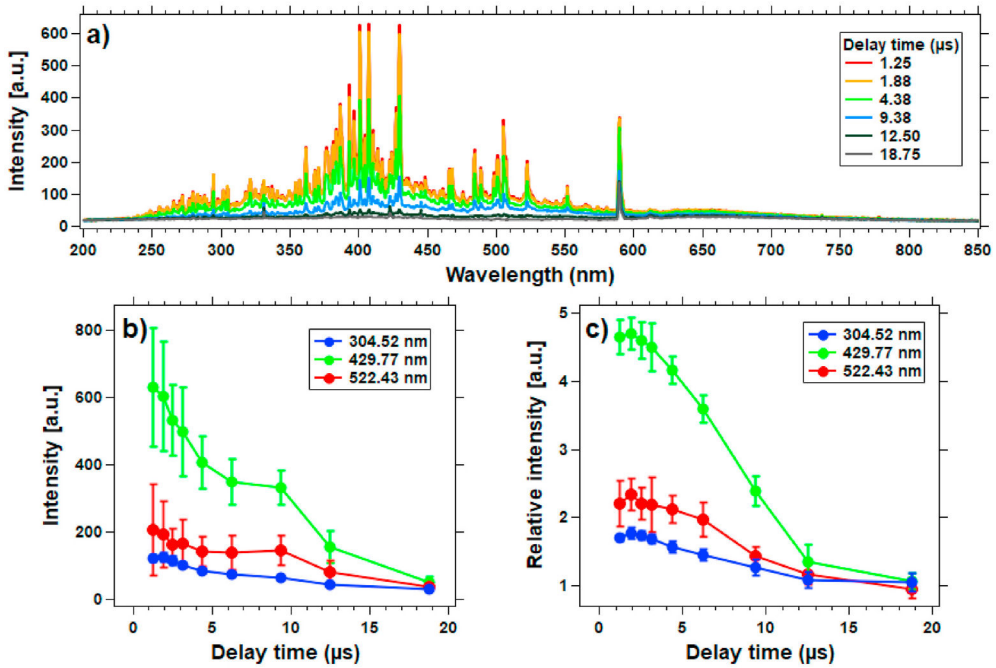

Fig. 2.

Spectra acquired between 1–20 μs after the spark discharge. (a) the original spectra collected after different delay times, (b) temporal behavior of intensities for representative tungsten emission lines, and (c) temporal behavior of relative intensities (i.e., after baseline correction) for representative tungsten emission lines. Each experimental condition was repeated ten times to calculate mean values and standard deviations.

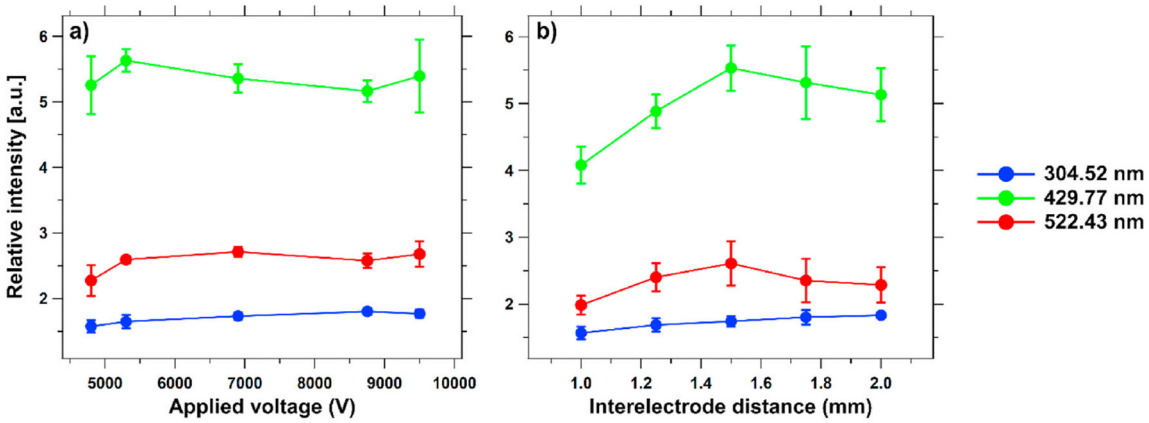

Fig. 3.

Relative intensities for representative tungsten emission lines under different (a) applied voltages and (b) interelectrode distances. Each experimental condition was repeated ten times to calculate mean values and standard deviation.

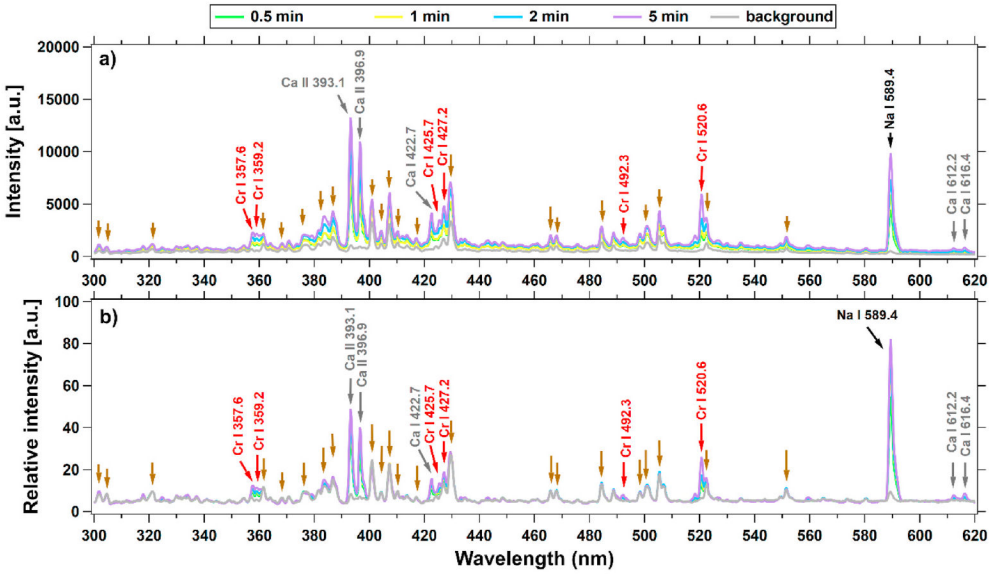

Fig. 4.

SIBS results for the analysis of Cr (aqueous solution of $Cr(NO_3)_3$, 2 μg ml^{-1}). In the figure, each spectrum is the average result of at least three repeated experiments. The brown arrows indicate strong emission lines of W. A zoomed plot of wavelengths from 380 to 420 nm can be found in Fig. S6.

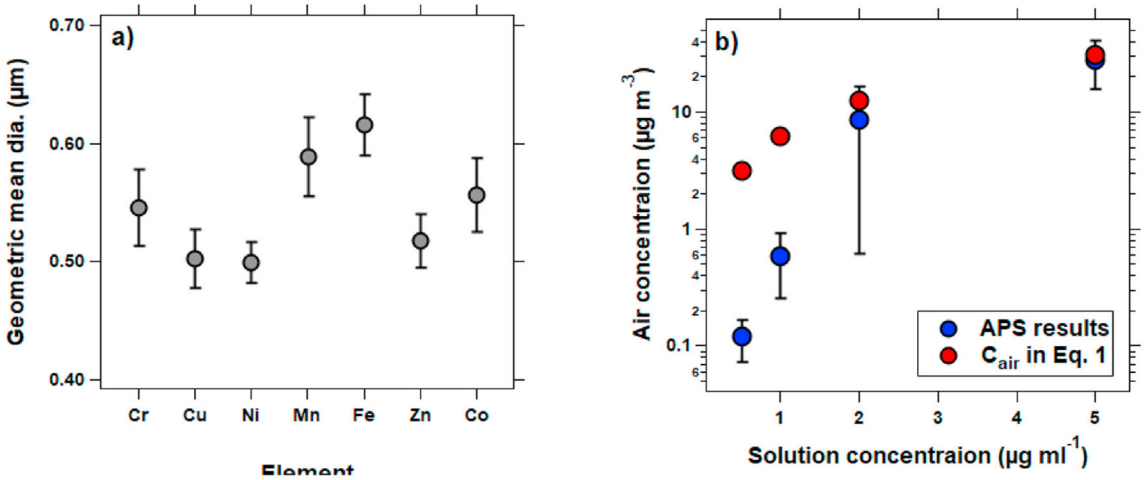

Fig. 5.

APS results of the heavy metals: (a) Geometric mean diameter of the tested metals and (b) Comparison of the mass concentration derived by APS and the calculated C_{air} in Eq. (1). For each element in panel (a), the error bar represents the standard deviation derived from the aqueous solutions of different concentrations (e.g., 0.5, 1, 2, and 5 μg ml^{-1}). For each level of solution concentration in panel (b), the error bar represents the standard deviation derived from different types of metal.

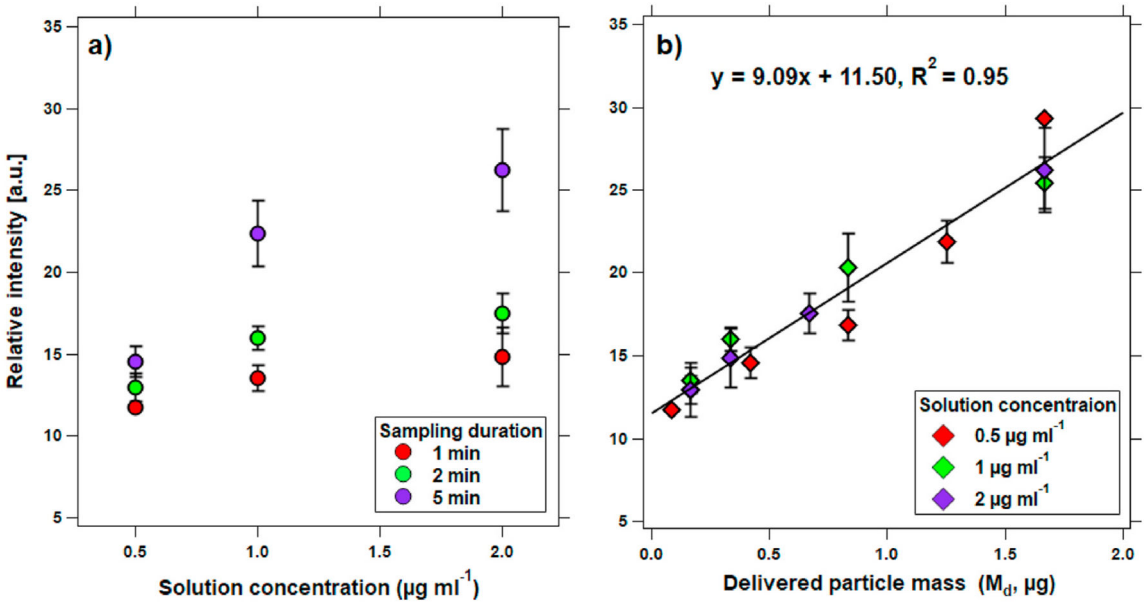

Fig. 6.

Calibration curve of Cr (520.6 nm): relative intensity as a function of (a) solution concentration with different sampling durations and (b) delivered particle mass by the nebulizer. Each experimental condition was repeated at least three times to calculate mean values and standard deviation. Similar to Fig. 4, the relative intensity is the sum of five sparks after each particle loading period.

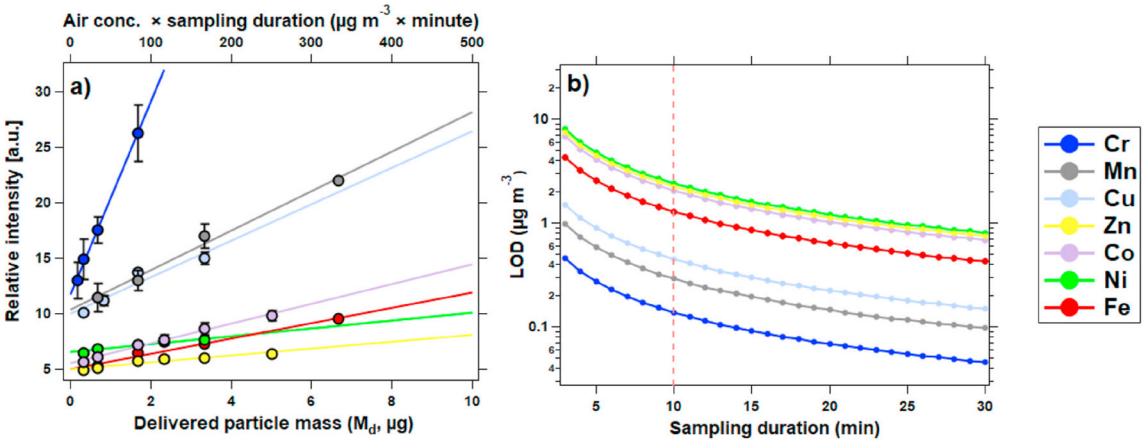

Fig. 7.

Quantitative results for different heavy metals. (a) calibration curves: relative intensity vs. M_d (bottom axis) or C_{air} × sampling duration (top axis), and (b) simulated LOD as a function of sampling duration (assuming an air flow rate of 15 l min^{-1}). In panels (b), the dashed line represents the condition used to derive the last column of Table 3.

Table 1

Experiment apparatus and settings used in the SIBS system.

Component	Parameter/model number and manufacture
Spark generation	
Capacitor	0.1 μF, 8000 V DC
Boost converter	35 W, 24 V DC input, 1000–10000 V DC output
Mechanical relay	8000 V DC
Tungsten electrodes	anode: a shaft diameter of 500 μm and a sharp tip diameter 50 μm; cathode: flat tip with 1 mm diameter
Delay generator	
Digital potentiometer	AD5241 (Analog Devices Inc.)
Differential comparator	LM311-N (Texas Instrument Inc.)
Pulse width modulation controller	LTC 6994 (Analog Devices Inc.)
Spectra collection	
Spectrometer	USB 2000 with an optical resolution of 0.35 ± 0.05 nm and a spectral range of 200–900 nm (Ocean Optics Inc.). During analysis, the integration time was set to be 3 ms (the lower boundary of the spectrometer software).
Optical fiber	M92L02, 250–1200 nm (Thorlabs Inc.)
Lens	LB4330, 75 mm focal length, 25.4 mm diameter (Thorlabs Inc.)
Photodiode	DET36A2, 350-100 nm (Thorlabs Inc.)

Table 2

Summary of the tested heavy metals and their chemical characteristics reported in the previous studies[a].

Element	Solution composition	Density (g cm^{-3})	Detection wavelength (nm)[b]	Instrument[c]	LOD (μg m^{-3})	Reference
Cu	$Cu(NO_3)_2$	3.05	324.48[d], 521.82[e]	SIBS	0.26	Zheng et al. (2018a)
Cr	$Cr(NO_3)_3$	1.89	520.6[d], 534.58[e]	SIBS	0.36	Zheng et al. (2018a)
Mn	$C_4H_6MnO_4$	1.59	257.6, 403.08[d,e]	SIBS	0.36	Zheng et al. (2018a)
Zn	$Zn(NO_3)_2$	2.06	213.8, 481.05[d,e]	SIBS	0.42	Zheng et al. (2018a)
Ni	$Ni(NO_3)_2$	2.05	352.45[e], 356.89[d]	SIBS	0.70	Zheng et al. (2018a)
Fe	$Fe(NO_3)_3$	1.64	373.55[d], 526.95[e]	SIBS	0.78	Zheng et al. (2018a)
Sb	Sb	6.68	259.81[e], 323.25	LIBS	120	Zhang et al. (1999)
As	As	5.7	278.02[e]	LIBS	600	Zhang et al. (1999)
Hg	HgO	11.14	253.65[e], 436.83	LIBS	680	Zhang et al. (1999)
Cd	$Cd(NO_3)_2$	3.6	326.11[e]	LIBS	120	Zhang et al. (1999)
			537.81[e]	SIBS	0.26	Zheng et al. (2018a)
Pb	$Pb(NO_3)_2$	4.53	405.78[e]	LIBS	68	Zhang et al. (1999)
			405.78[e]	SIBS	0.80	Zheng et al. (2018a)
Co[f]	$Co(NO_3)_2$	1.87	340.9, 345.1[d]	–	–	–
Se[f]	SeO_2	3.95	241.35	–	–	–

[a] Results are ordered by the LOD specified by the previous studies, except for Pb and Cd.

[b] For each element, only one or two representative emission lines are given in the table.

[c] Note that the SIBS system used in Zheng et al. (2018a) differs from ours in that they created an electrical field when collecting particles. See section 2.1 for more details.

[d] The emission line used by the present study to determine LOD of the tested metal.

[e] The emission line used by the study listed in the last column of the table to determine LOD.

[f] To our knowledge, there has not been any reports of the LOD of Co and Se using aerosols nebulized from aqueous solution.

Table 3

Summary of the calibration results of heavy metals.

Element	Detection wavelength (nm)	Regression	R^2	LOD (μg)[a]	LOD (μg m^{-3})[b]
Cr	520.6	y = 8.72x + 11.71	0.95	0.03	0.14
Mn	403.08	y = 1.79x + 10.37	0.99	0.04	0.29
Cu	324.48	y = 1.65x + 9.93	0.90	0.07	0.45
Fe	373.55	y = 0.69x + 5.00	0.99	0.19	1.3
Co	345.1	y = 0.89x + 5.47	0.99	0.31	2.1
Zn	481.05	y = 0.41x + 0.41	0.92	0.33	2.3
Ni	356.89	y = 0.31x + 6.46	0.92	0.36	2.4

[a] LOD is expressed as the mass of particles delivered by the air sampling system (μg).

[b] LOD is expressed as of air concentrations (μg m^{-3}) by assuming a sampling duration of 10 min and a flow rate of 15 l min^{-1} (same as our experimental condition).